Deep-tissue label-free quantitative optical tomography

van der Horst, Jelle; Trull, Anna K.; Kalkman, Jeroen

DOI
10.1364/OPTICA.397549

Publication date
2020

Document Version
Final published version

Published in
Optica

Citation (APA)
van der Horst, J., Trull, A. K., & Kalkman, J. (2020). Deep-tissue label-free quantitative optical tomography. *Optica*, *7*(12), 1682-1689. https://doi.org/10.1364/OPTICA.397549

optica

Deep-tissue label-free quantitative optical tomography

JELLE VAN DER HORST, ANNA K. TRULL, AND JEROEN KALKMAN*

Department of Imaging Physics, Delft University of Technology, Lorentzweg 1, 2628 CJ Delft, The Netherlands
**Corresponding author: j.kalkman@tudelft.nl*

Received 26 May 2020; revised 1 October 2020; accepted 2 October 2020 (Doc. ID 397549); published 30 November 2020

In vivo **imaging of small animals is of wide interest to the biomedical community studying biological disease and developmental processes. However, optical imaging deep in tissue is severely limited by light scattering, posing restrictions on the imaging depth, image contrast, and spatial resolution. We demonstrate optical coherence projection tomography (OCPT) as a fast three-dimensional optical imaging technique for ballistic, non-scattered light, deep-tissue imaging. OCPT is based on a novel scanning transmission sample arm to rapidly measure ballistic light projections of amplitude and phase through thick biological tissues. We demonstrate the strength of OCPT by imaging an adult zebrafish in a total volume of 1000 mm^3 acquired in 24 min. We achieve an unprecedented imaging depth of 4 mm in biological tissue without using optical clearing (up to 27 mean free paths of photon transport). A new way of analyzing optical tomographic imaging depth is demonstrated and applied to OCPT. It shows that the strong light scattering suppression in OCPT is pivotal to reach the SNR limited imaging depth. OCPT allows for a full quantitative assessment of tissue parameters, which is demonstrated by quantifying the attenuation coefficient, refractive index, surface area, and volume of various organs deep inside the zebrafish. Our work opens up the way for longitudinal** ***in vivo*** **small animal studies from the larval to the adult stages.**

https://doi.org/10.1364/OPTICA.397549

1. INTRODUCTION

The ability to image deep-lying layers of biological tissue in a non-invasive fashion holds great promise for biological and biomedical studies. To achieve this, the scientific challenge is to prevent light scattering inside the tissue from degrading the optical imaging depth, image contrast, and spatial resolution. Various techniques have been developed to tackle this problem either by reducing the amount of light scattering—for example, through optical tissue clearing [1,2] or by using long-wavelength multi-photon imaging [3–5]—or to selectively detect ballistic (unscattered) light—for example, through confocal detection [6], gating based on coherence of the collected photons [7], gating based on photon arrival times [8,9], or decoupling illumination and detection [10,11]).

One of the most successful approaches for imaging in turbid media is optical coherence tomography (OCT) [12,13], which is efficient in the selective detection of ballistic, single-scattered light for low scattering media. However, for highly scattering media, photons are mapped onto a depth matching their optical path length (OPL) that, for the majority of photons, is not equal to the single scattering path length. This results in reduced image contrast and reduced signal-to-noise ratio (SNR) [14,15].

In contrast to reflection-based imaging geometries, in transmission, not the weak backscattered light is detected, but instead all the transmitted light is collected by the exit numerical aperture (NA). Moreover, the optical path-length distribution (OPLD) measured in transmission is free from the ambiguity of path length and reflection depth that is present in OCT imaging of dense scattering media [14]. Therefore, selection of only ballistic photons from the transmitted light can be performed by path length selection [16,17]. A disadvantage of path-length-resolved transmission OCT imaging is that no direct 3D spatial information is obtained. Instead, path-length-integrated measurements of spatially varying optical properties have to be processed using computed tomography to reconstruct 3D images.

Several transmission-based optical tomographic techniques have been reported, using either time gating or confocal gating [18–20]. Some techniques focus only on group-refractive-index-based imaging of transparent phantom samples [18,21]; others allow attenuation-based imaging of turbid materials but are not quantitative [19] or do not use ballistic light selection for high-resolution imaging [20]. All are based on slow lateral scanning with translation stages making their application cumbersome. Hence, the applied gating techniques for transmission imaging are not used to their full potential.

Here, we present optical coherence projection tomography (OCPT) as an optical imaging modality that addresses these issues in a novel way through the use of a rapidly scanning transmission sample arm for both amplitude- and phase-resolved detection of ballistic photons. We demonstrate label-free deep-tissue quantitative imaging up to a depth of 4 mm in tissue, corresponding to 27 mean free paths (MFPs).

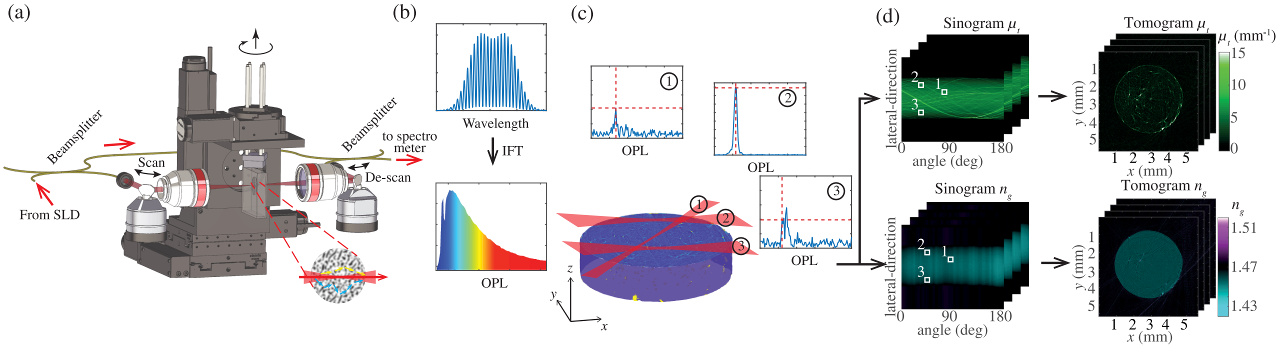

Fig. 1. General principle of OCPT imaging. (a) Fiber-based spectral-domain transmission OCT system with scanning sample arm. (b) Optical path length (OPL) distributions are computed from the measured interference spectra. Based on the OPL distribution, the signal from ballistic photons is selected and used for imaging. (c) Multiple transmission measurements are taken from different lateral positions and angles, illustrated here by measurements of a scattering silicone phantom. (d) For each measurement of (c), an OPL distribution is computed, and the height and location of the ballistic signal are analyzed and ordered into sinograms for the attenuation coefficient μ_t and group refractive index n_g. Finally, 3D images of these optical properties are reconstructed from the sinograms (see Visualization 1).

2. OCPT METHODOLOGY

The general concept of OCPT is depicted in Fig. 1. Transmission measurements are performed with a single-mode fiber-based spectral-domain low-coherence interferometer system operating at a center wavelength of 1300 nm with a sensitivity of -116 dB and a coherence length of 29 µm [see Fig. 1(a) and Section 1 in Supplement 1]. Light from the sample arm of a Mach–Zehnder interferometer is focused in the sample, and transmitted photons are collected with a lens and coupled into a single-mode fiber. The sample arm consists of a novel rapidly scanning and de-scanning galvanometer system. The scanning is synchronized with the de-scanning to achieve high transmission over the entire 8 mm lateral range of the projection (see Section 2 in Supplement 1) and enables acquisition of a single projection in 20 ms. The collected transmitted sample arm light is combined with light from the reference arm, and the resulting interference pattern is measured on a spectrometer. From the interference spectrum, the OPL distribution of the light transmitted by the sample is calculated through an inverse Fourier transform, as shown in Fig. 1(b).

Ballistic photons that travel straight through the object accumulate on the shortest optical path and create a sharp peak in the OPL distribution [see Fig. 1(b)]. Non-ballistic photons are scattered in the sample and therefore travel longer distances resulting in their detection as a distribution with longer path lengths than the ballistic peak in the OPL distribution. For selection of ballistic signal photons, only photons that travel the shortest straight optical through the sample are detected. Relative to an empty sample arm, the height and location of the ballistic peak are a measure of the path-length-integrated attenuation coefficient and group refractive index of the sample, respectively.

OCPT is based on the rapid sequential point scanning of transmission measurements from different angles and lateral shifts. From these measurements, the 3D distributions of the group refractive index, n_g, and attenuation coefficient, μ_t, are reconstructed. Although μ_t encompasses both absorption and scattering, for biological tissues imaged in the used wavelength band, absorption is negligible, and μ_t gives primarily scattering contrast information. Figures 1(c) and 1(d) demonstrate this process with measurements of a scattering silicone phantom (see Section 3 in Supplement 1). The collected ballistic transmission peak heights and OPL positions are ordered in two separate sinograms that are reconstructed independently using the algebraic reconstruction technique (ART) [22] (see Section 4 in Supplement 1 for a detailed description of the signal processing steps). The cylindrical phantom has a diameter of approximately 4 mm, mean attenuation coefficient of $1.3 \pm 0.8\ \mathrm{mm}^{-1}$, and mean group refractive index of 1.463 ± 0.001. The sinograms of the two modes of contrast [Fig. 1(d), right] reveal clear differences, as do the reconstructed 2D tomograms [Fig. 1(d), left]. The attenuation coefficient image shows the structure of the object and many strongly scattering clusters of titanium dioxide. The refractive index image shows a homogeneous refractive index within the phantom. Some of the larger clusters of titanium dioxide are also visible in the refractive index image (for full 3D images, see Visualization 1).

3. OCPT IMAGING OF TISSUE PHANTOMS

OCPT is based entirely on ballistic light and, as a result, the spatial resolution is not affected by scattering in the sample. Instead, it is determined solely by the imaging system specifications. The tomographic image resolution is determined experimentally from the images of the individual titanium dioxide clusters in the silicone phantom. The titanium dioxide clusters, reported as having a mean diameter of 730 ± 600 nm [23], can be considered point objects for OCPT. The phantom material was measured in 64 transverse slices spaced 8 µm apart. Each slice was measured with 1000 lateral sampling points covering 8 mm, and 180 angular projections with a sampling distance of 1°. The individual clusters in the OCPT image of the phantom, which is shown in Fig. 1(d), are characterized by their full width at half maximum (FWHM) in the radial, tangential and vertical directions (see Section 6 in Supplement 1, which describes a full characterization of the position-dependent resolution in the attenuation coefficient OCPT image). The resolution of OCPT images is anisotropic, varying with position in the image, which is caused by the limited depth of field of the imaging system, an effect that has been studied extensively for optical projection tomography (OPT) [24]. Our analysis shows an isotropic 20 µm FWHM resolution at the center of the image. At 1 mm from the center, the resolution in the tangential direction degrades to 100 µm at 1.5 mm from the center. The resolution in

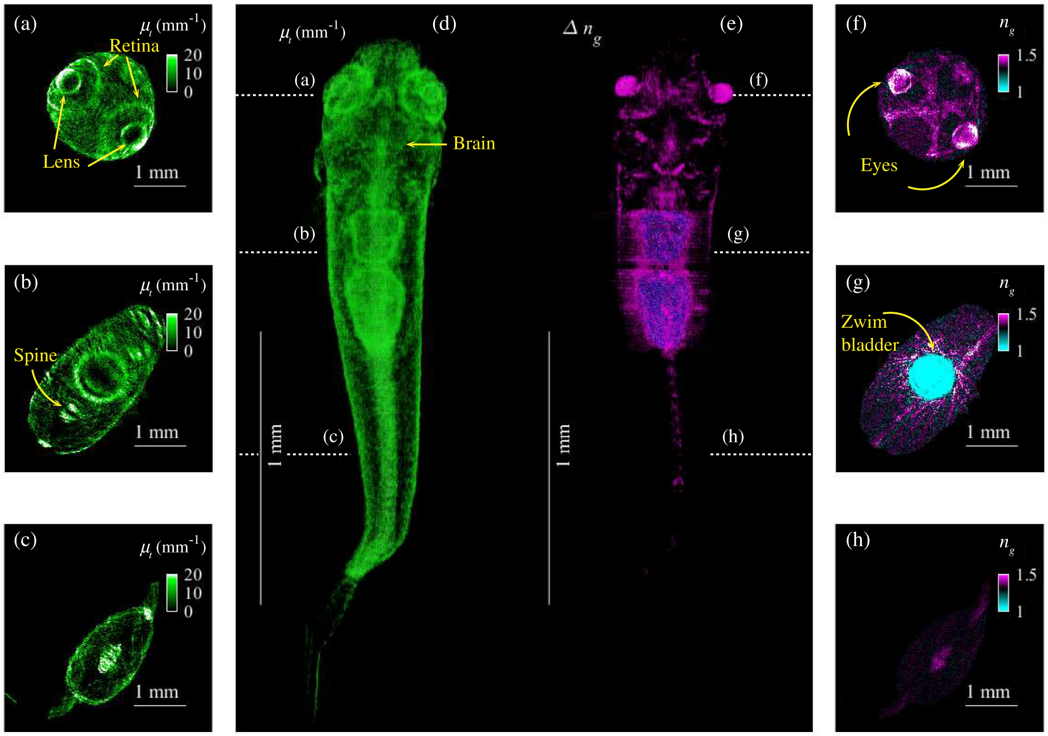

Fig. 2. OCPT imaging of an adult zebrafish. Reconstructed transverse tomograms of the (a)–(c) absolute attenuation coefficient μ_t and (f)–(h) group refractive index n_g of an adult zebrafish. False-colored 3D visualizations for the (d) attenuation coefficient and (e) group refractive index in a coronal plane of the zebrafish.

the radial and vertical directions does not degrade with distance from the center.

Validation measurements of the quantitative image contrast were performed with an agarose cylinder imaged with OCPT while immersed in water-diluted Intralipid solutions. The addition of Intralipid to water changes both the refractive index as well as the attenuation of the medium. The optical properties of the Intralipid–water mixture are determined in bulk using transmission OCT [17] and compared with the values obtained in the OCPT images. Both values are in good agreement (see Section 5 in Supplement 1).

4. OCPT IMAGING OF AN ADULT ZEBRAFISH

Zebrafish larvae are imaged extensively as model animals in medical and biological research due to their easy maintenance, rapid reproduction, and optical transparency. In contrast, adult zebrafish are larger and not as transparent as the larvae and therefore challenging to fully image in 3D at high resolution. Experiments were performed on adult zebrafish mounted in 2% low-melting point agarose gel that was encased in tube of 4 mm inner diameter fluorinated ethylene propylene tube. Before fixation in agarose, the zebrafish were euthanized in ice water in the Erasmus University Medical Centre Rotterdam (Erasmus MC) according to animal welfare regulations. A total of 200 transverse slices were recorded, uniformly distributed over 20 mm. The lateral and angular sampling was the same as presented for the phantom experiments. The total 3D volume of 1000 mm^3 was obtained in 24 min during which 137 GB of raw data was acquired.

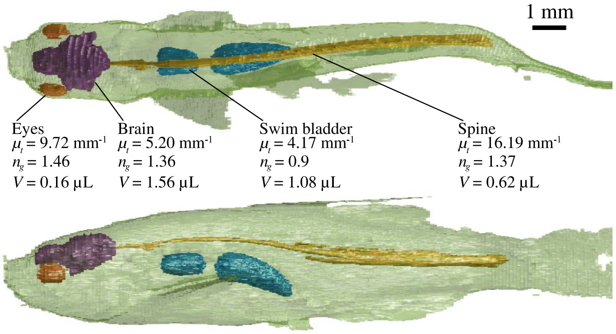

Fig. 3. Quantification of zebrafish tissue optical properties imaged with OCPT. Segmentation of multiple zebrafish organs with volume and median optical properties of the eyes, brain, spine, and swim bladder.

Figure 2 shows the full OCPT imaging of a 4 mm thick, 20 mm long adult zebrafish embedded in agarose. Figures 2(a)–2(c) show transverse cross sections of the zebrafish attenuation coefficient. Several distinct anatomical features can be recognized such as the eye lens and retina, the swim bladder, and the spine. The group refractive index images of the zebrafish are shown in Figs. 2(f)–2(h). The group refractive index transverse cross sections show several anatomical features of the fish. The gas-filled swim bladder ($n_g = 1$) is clearly visible from the surrounding tissue that has a higher refractive index. The lenses of the eyes also show high contrast. False-colored 3D visualizations of the zebrafish attenuation coefficient and group refractive index [Figs. 2(d) and 2(e) and Visualization 2, Visualization 3] show the spine, brain, and overall structure of the zebrafish.

With OCPT, quantitative analysis of tissue and organ properties in toto is realized. Figure 3 shows a representative example of this approach visualizing the zebrafish brains, eyes, skin, spine, and

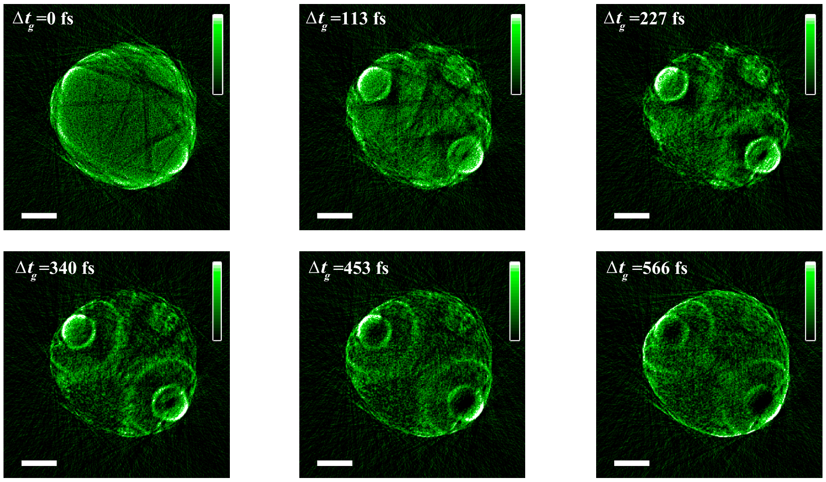

Fig. 4. Fixed time gate OCPT reconstructions. Application of fixed time gating to the OPLD for several time windows measured with OCPT on zebrafish.

swim bladder segmented with different methods based on OCPT images of the group refractive index or attenuation coefficient (as described in Section 7). From the segmented organs, their surface area, volume, and median optical properties are calculated. With OCPT, quantitative label-free assessment of tissue development and function at high resolution in an adult uncleared zebrafish is realized, something that is unfeasible with current state-of-the-art imaging equipment.

In addition, we demonstrate the ability to create fixed-time coherence-gated OCPT reconstructions, as shown in Fig. 4, which shows μ_t reconstructions for light arrival times varying between 0 and 566 fs. These images with variable time gates are computed by integrating the measured intensity in the OPLD within a Gaussian window with a FWHM corresponding to 63 fs travel time in air. The figure shows that different positions of the fixed-time coherent gate result in changes in the visible anatomical features. The release of the coupling between ballistic light and attenuation increases the attenuation contrast and also shows multiple scattered light in the reconstruction. Only with the Fourier-domain implementation of high-speed OPLD acquisition in OCPT does the adjustment of the arrival time not require any additional acquisition time and can be performed after data acquisition.

5. OCPT IMAGING DEPTH ANALYSIS

For optical imaging techniques, the imaging depth increases with: (1) increasing system sensitivity and (2) stronger rejection of scattered light. The precise trade-offs between these two parameters and the effect of the sample properties make it complicated to determine the exact imaging depth *a priori* [25].

A. Sensitivity Limited Imaging Depth

In the case of sufficient suppression of multiple scattered light, the maximum imaging depth is defined as the number of MFP lengths of photon transport for which the SNR becomes one. The SNR is defined as $\mathrm{SNR} = 10\log_{10}(P_0/P_{\mathrm{noise}})$, where P_0 and P_{noise} are the signal and noise powers, respectively. Hence, the maximum imaging depth for a backscatter-based low-coherent imaging system is given by

$$z_{\mathrm{backscat}} = \frac{1}{2}\left[\ln(l_s\, p_{\mathrm{NA}}\mu_s) + \frac{\mathrm{SNR}_{\mathrm{dB}}}{10}\ln 10\right], \qquad (1)$$

where l_s is the coherence length, p_{NA} is the scattering phase function integrated over the collection NA of the imaging system lens, and μ_s is the scattering coefficient of the sample [26]. The first term in Eq. (1) describes that only a fraction of the scattered light is scattered in the backward direction, limiting the signal received by a backscatter-based system. For a system with coherence length $l_s = 10$ µm, SNR $= 116$ dB, $p_{\mathrm{NA}} = 4 \cdot 10^{-5}$, and $\mu_s = 4\ \mathrm{mm}^{-1}$, this results in a maximum imaging depth $z_{\mathrm{OCT}} = 7$ MFP.

Imaging in transmission, as is the case for OCPT, the first factor in Eq. (1) is eliminated since all unscattered transmitted light can contribute to the detected signal. Moreover, due to the absence of a return path through the sample, the factor 1/2 is also absent, effectively increasing the imaging depth by a factor of two. Hence, the OCPT sensitivity limited imaging depth is

$$z_{\mathrm{OCPT}} = \left[\frac{\mathrm{SNR}_{\mathrm{dB}}}{10}\ln 10\right]. \qquad (2)$$

Consequently, transmission-based imaging has a much larger imaging depth than conventional backscatter-based imaging. For a transmission low-coherence system with a sensitivity of -116 dB, the maximum imaging depth would be $z_{\mathrm{OCPT}} = 27$ MFP, which is almost a factor of four larger than the imaging depth computed for a backscatter-based imaging system. In addition, the transmission system does not suffer from the path length ambiguity of multiple scattered optical paths mapping onto shallower depths [14] that backscatter-based imaging systems have.

B. Multiple Scattering Limited Imaging Depth

For the case of strong multiple scattering, the imaging depth is given by the ratio of detected ballistic to diffuse power, which, for a transmission confocal system and a homogeneous sample, is given by [25]

$$R_{\mathrm{bd}} = \frac{\pi L^2}{2\lambda^2}\mu_s(1-g)L\exp(-\mu_s L), \qquad (3)$$

where L is the sample thickness, g the scattering anisotropy, and λ the light wavelength. Based on Eq. (3), using the same parameters as above, $\lambda = 1300$ nm, and taking a typical value of $g = 0.9$ in tissue, the detected ballistic power equals the scattered light power for a transmission confocal system at $L = 17.2$ MFP. An increase to 21.5 MFP has been measured in a transmission confocal system with a narrow bandwidth heterodyne detection [25]. Considering the sensitivity limit $z_{\mathrm{OCPT}} = 27$ MFP of our OCPT system, only a confocal gating would not sufficiently reject scattered light to guarantee ballistic imaging. Consequently, the coherence and time gating applied in OCPT are required to sufficiently reject scattered light in the imaging process.

Considering the suppression of multiple scattered light, OCPT suppresses scattered light in three ways. First, multiple scattered photons are filtered out since they do not couple efficiently to the single-mode fiber that acts as a collection pinhole (confocal gating). Second, photons that due to scattering lose their polarization or are not coherent anymore with the single spectral pixel temporal coherence do not contribute to the measured interference signal and are also suppressed in the image formation (combined confocal interference gated detection). Third, the path length selection identifies ballistic photons based on their path length and hence on their arrival time (full spectral bandwidth coherence/time gating). The contributions of the confocal gate, confocal and interference gates, and coherence/time gate to the imaging depth can be separated experimentally by reconstructing images with different input signals all derived from the same OCPT data set (as described in Section 4 of Supplement 1).

The deep-tissue OCPT imaging performance is analyzed in a novel way by determining the optical thickness distribution for all rays in the measured attenuation sinogram. The optical thickness is the mean number of MFPs, i.e. $p_{\mu_t}(\theta, t) = \int \Delta\mu_t(s, t)\mathrm{d}s$ for all, and is an indication of the maximum imaging depth of the imaging system. In order to reduce the effects of noise, the calculations are performed using a sinogram that is computed from the reconstructed data $\mu_t(x, y, z)$ using the Radon transform $\mathcal{R}$. With the forward projected sinogram, $p_{\mu_t \mathrm{back}}(\theta, t, z) = \mathcal{R}\mu_t(x, y, z)$ rays are taken into account that in principle cannot be measured because of Eq. (1), but that are reconstructed based on other rays that travel through the sample. This analysis is corroborated by comparing the forward projected attenuation sinogram with the attenuation sinogram obtained directly from the measurements $\Delta p_{\mu_t}(\theta, t, z) = |p_{\mu_t \mathrm{back}} - p_{\mu_t}|$. A deviation of the measured sinogram with the forward projected sinogram means that the ray measurement is not consistent with the overall object reconstructed from all the rays, indicating a measurement error. An estimate of the maximum imaging depth is made by computing how many rays of the forward projected sinogram deviate significantly (>50%) from the corresponding measured sinogram rays.

The confocal gated attenuation image of a single slice of the zebrafish brain in Fig. 5(a) shows poor image quality due to weak rejection of multiple scattered light. The image clearly shows the outline of the zebrafish, but no inner structures can be observed. The MFP distribution of the measured rays for confocal gated tomographic imaging is shown in Fig. 6(a). The MFP distribution, terminates in the 10–12 MFP region. In confocal detection, some of the scattered light is not rejected, causing the detected signals to be higher than the ballistic OCPT signal. This results in an underestimation of the attenuation, hence limiting the sampled MFP range. The analysis of inconsistent rays, shown in Fig. 6(b), indicates a sharp increase in inconsistent rays at 12 MFP, which is at the end of the confocal gated imaging range. Inconsistencies at low MFPs are caused mainly by detector saturation errors.

The confocal and interference gated attenuation image, shown in Fig. 5(b), shows many more internal structures of the zebrafish. The addition of the interference gate improves the image quality, and fewer multiple scattered photons are measured. In Fig. 6(a), the MFP distribution also shows an increase in rays with a larger optical thickness, indicating a higher sensitivity, and terminates in the 13–15 MFP range. For the confocal and coherence gated images, a sharp increase in inconsistent rays in observed at 14 MFP, shown in Fig. 6(b), which is at the end of the confocal and coherent gated imaging range. This imaging performance is better than imaging with confocal gating only. The improvement in image quality of the confocal image with the addition of the interference gate is attributed to the increase in heterodyne sensitivity of the system and improved suppression of scattered light that has the wrong polarization or path length.

The OCPT attenuation image in Fig. 5(c) shows an improvement in image contrast compared to the confocal and confocal with interference gated images and clearly reveals the most structural features inside the zebrafish. As OCPT image reconstruction is done by ballistic light selection in the OPL distribution, the addition of the coherence/time gate to select only ballistic light is crucial to achieve high contrast deep in tissue. This is especially important since for biological tissue, light scatters primarily in the forward direction [27] leading to a rapid deterioration when imaging through thick tissue without sufficient suppression of multiple scattered light. In addition, the measured attenuation values are higher due to the improved suppression of scattered light. The MFP histogram in Fig. 6(a) shows that the majority of the rays is

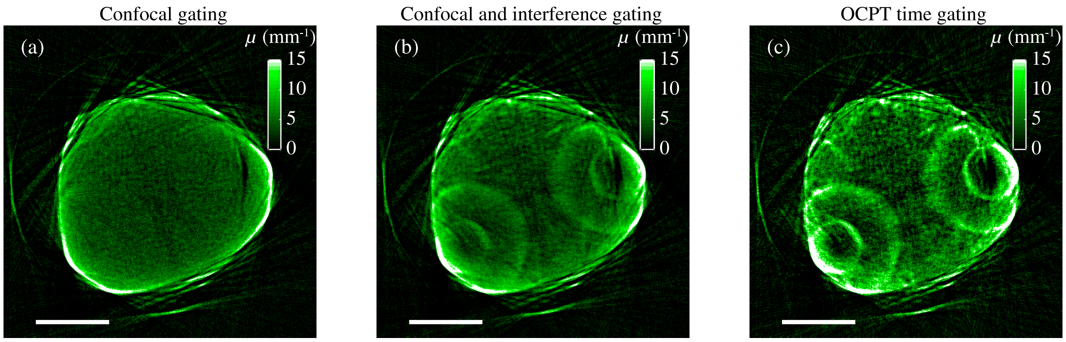

Fig. 5. Comparison of different gating methods in optical tomographic imaging. (a) Confocal gated tomographic image. (b) Tomographic image created by a combination of confocal gating and interference gating. (c) OCPT image made by combining confocal gating, interference gating, and time gating. Scale bar 1 mm.

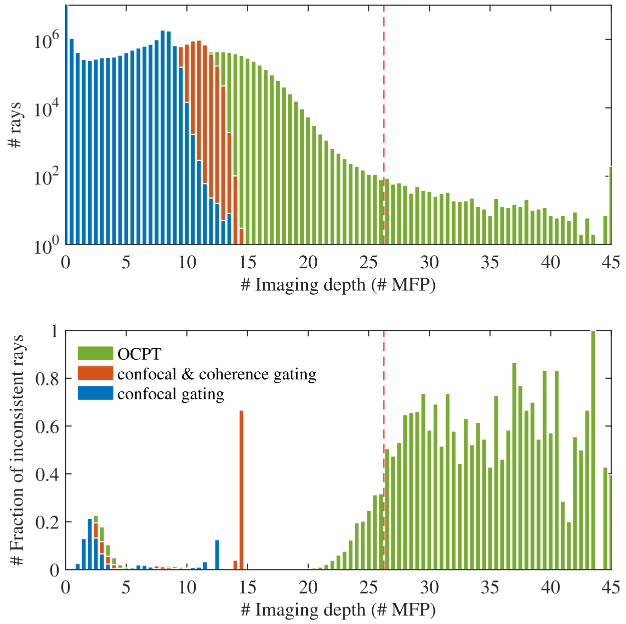

Fig. 6. Analysis of the OCPT imaging depth. (a) Histogram of the optical thickness for every computed ray through the measured tissue as a function of the MFP traversed by the ray for OCPT, confocal imaging and confocal imaging with coherence gate. The dashed red line indicates z_{OCPT}. (b) The fraction of rays for which the computed sinogram with path-length-integrated attenuation coefficients deviates from the directly measured sinogram by more than 50%.

within the limit computed for transmission OCT using Eq. (1). The background medium contributes a large number of rays with approximately close to zero MFP of optical thickness. A small fraction of the rays show MFP values higher than the system sensitivity limit. This is attributed to the tomographic reconstruction process in which the volume sampled by rays experiencing large attenuation is measured indirectly by rays propagating from directions that have smaller integrated attenuations. Consequently, the full object is reconstructed, even though it is optically thicker than z_{OCPT} at some angles and lateral positions. Not taking this effect into account, the maximum imaging depth z_{OCPT} is clearly visible from the fast increase in incorrect rays, observed at 27 MFP, the maximum OCPT imaging depth. This depth is in good agreement with the prediction of z_{OCPT} based on Eq. (2). From this analysis, it follows that OCPT pushes the ballistic light scattering imaging to its fundamental SNR-limited range of 27 MFPs, equivalent to the detection of a fraction as small as 10^{-12} of the input light.

6. DISCUSSION

With its 27 MFP imaging depth, OCPT outperforms many state-of-the-art deep-tissue imaging techniques.

Compared to reflection optical imaging systems [28] such as OCT and confocal microscopy, transmission systems, such as OCPT, have a more efficient use of the OPL through the medium, more efficient light collection, and no path length depth ambiguity. In contrast to wavefront-based techniques for deep-tissue imaging (such as wavefront shaping [29,30], time reversal [31,32], and coherent addition [33]), OCPT is not based on phase conjugation and is therefore not affected by movements on the order of a wavelength during a single acquisition. Hence, OCPT can be applied to objects that have sub-resolution movement due to, e.g., blood flow or heart beats.

In its generated images OCPT resembles those obtained with optical coherence refraction tomography (OCRT) [34]. However, in contrast to OCRT, OCPT provides quantitative attenuation contrast and is capable of deeper imaging due to the single-pass geometry. On the other hand, OCPT light rays do suffer from refraction, which is currently not taken into account. Similar to OCRT, this issue can be addressed using iterative reconstruction based on the initial refractive index reconstruction.

OCPT is the Fourier-domain equivalence of time-gated OPT (TG-OPT) [9]. OCPT has approximately equivalent imaging depth as TG-OPT. However, TG-OPT is performed with higher sampling in the axial direction, thereby yielding better image quality in sagittal planes through the zebrafish. However, because of the variable time gate, OCPT allows for multi-parameter quantitative imaging of μ_t and n_g, providing better contrast in the image.

A. OCPT Speed and Resolution

OCPT can build on the many hardware innovations and methodological advances made in the field of OCT and fiber technology. Further speed improvements can be foreseen with the use of, for example, parallel transmission OCT using a line illumination and detection [35]. In combination with the same illumination power per lateral spot, this also can significantly increase the SNR.

In addition to the significantly improved contrast, the selection of the ballistic light results in a sample-independent resolution. In OCPT, the spatial resolution is determined entirely by the imaging optics. Consequently, OCPT can image with high and isotropic resolution in the center, but suffers from a decrease far away from the center due to the limited depth of field. Potential resolution improvement can be achieved through the use of divergence-free Bessel beams. Alternatively, point-spread-function based reconstruction [36] can be performed, which is compatible to the present case of a shift variant PSF of our scanning transmission sample arm.

Besides application to OCPT, we envision the rapid scanning transmission sample arm to be relevant to other imaging techniques that are currently configured in reflection geometry. The implementation of the scanning transmission sample arm can improve the signal collection efficiency and/or improve the imaging contrast in scanning imaging modalities such as confocal microscopy, phase contrast microscopy, second-harmonic imaging, and multi-photon microscopy.

B. OCPT Applications

OCPT allows for high-speed quantitative 3D imaging of turbid objects without the need for optical clearing or labeling. The total acquisition time of 24 min makes it feasible to perform measurements on an entire sedated live zebrafish. In this way, OCPT has the potential for longitudinal high-resolution *in vivo* imaging of a zebrafish from the larval to the adult stage. In a more optimized setting, such as through the use of full automation of zebrafish sorting, transport, rotation, and imaging, OCPT high throughput zebrafish imaging can be realized. Based on the OCPT tissue contrast, many adult zebrafish organs can be visualized, segmented, and quantified.

OCPT presents an advancement over current imaging techniques that focus mainly on small transparent zebrafish larvae. In high throughput microscopy of zebrafish larvae [37], the focus is on quantification of their exterior properties such as overall shape, volume, and surface area [38] without having sufficient contrast to quantify the interior of the fish. In contrast to OPT [37] and light sheet microscopy [39], OCPT can image larger and less transparent zebrafish. OCPT's combined $\Delta\mu_t$ and n_g contrast enables imaging and segmentation of internal organs in a single acquisition without the use of multi-modal imaging with fluorescent labeling [40]. OCPT has the ability for quantitative analysis of many zebrafish organs, which in combination with the potential for *in vivo* imaging makes it possible to perform quantitative longitudinal studies from the larval to the adult stage. This makes OCPT an interesting tool for many studies on drug efficacy, toxicity, and developmental biology.

7. CONCLUSION

OCPT provides a new and quantitative way for label-free quantitative deep-tissue imaging. It provides the first-ever quantitative measurements of optical properties of an entire adult zebrafish, thereby opening a broad range of new applications for (pre-clinical) research in the life science and medicine. The significant leap in imaging depth achieved with OCPT widens the possible range of optical imaging and could benefit the imaging of 3D cell cultures, tissue organoids, embryos, human biopsy tissues, small animals, plants, and optically cleared larger biological systems such as whole mice. OCPT is based on a novel scanning transmission sample arm to rapidly measure ballistic light projections of amplitude and phase through thick biological tissues with use in a wide variety of optical microscopy applications.

Funding. Nederlandse Organisatie voor Wetenschappelijk Onderzoek (12978).

Acknowledgment. The authors thank L. J. van Vliet for useful discussions and T. J. van Ham for his assistance with the zebrafish experiments.

Disclosures. The authors declare no conflicts of interest.

See Supplement 1 for supporting content. Data sets and analysis software are available at [41] or via the DOI:10.5281/zenodo.4138957.

REFERENCES

1. D. Zhu, K. V. Larin, Q. Luo, and V. V. Tuchin, "Recent progress in tissue optical clearing," Laser Photon. Rev. **7**, 732–757 (2013).
2. J. Sharpe, U. Ahlgren, P. Perry, B. Hill, A. Ross, J. Hecksher-Sørensen, R. Baldock, and D. Davidson, "Optical projection tomography as a tool for 3D microscopy and gene expression studies," Science **296**, 541–545 (2002).
3. W. Denk, J. H. Strickler, and W. W. Webb, "Two-photon laser scanning fluorescence microscopy," Science **248**, 73–76 (1990).
4. W. R. Zipfel, R. M. Williams, and W. W. Webb, "Nonlinear magic: multiphoton microscopy in the biosciences," Nat. Biotechnol. **21**, 1369–1377 (2003).
5. E. Papagiakoumou, A. Bègue, B. Leshem, O. Schwartz, B. M. Stell, J. Bradley, D. Oron, and V. Emiliani, "Functional patterned multiphoton excitation deep inside scattering tissue," Nat. Photonics **7**, 274–278 (2013).
6. J. Schmitt, A. Knüttel, and M. Yadlowsky, "Confocal microscopy in turbid media," J. Opt. Soc. Am. **11**, 2226–2235 (1994).
7. T. H. Nguyen, M. E. Kandel, M. Rubessa, M. B. Wheeler, and G. Popescu, "Gradient light interference microscopy for 3D imaging of unlabeled specimens," Nat. Commun. **8**, 210 (2017).
8. G. M. Turner, G. Zacharakis, A. Soubret, J. Ripoll, and V. Ntziachristos, "Complete-angle projection diffuse optical tomography by use of early photons," Opt. Lett. **30**, 409–411 (2005).
9. L. Fieramonti, A. Bassi, E. A. Foglia, A. Pistocchi, C. D'Andrea, G. Valentini, R. Cubeddu, S. De Silvestri, G. Cerullo, and F. Cotelli, "Time-gated optical projection tomography allows visualization of adult zebrafish internal structures," PLoS One **7**, e50744 (2012).
10. J. Huisken, J. Swoger, F. Del Bene, J. Wittbrodt, and E. H. Stelzer, "Optical sectioning deep inside live embryos by selective plane illumination microscopy," Science **305**, 1007–1009 (2004).
11. P. J. Keller, A. D. Schmidt, J. Wittbrodt, and E. H. Stelzer, "Reconstruction of zebrafish early embryonic development by scanned light sheet microscopy," Science **322**, 1065–1069 (2008).
12. D. Huang, E. A. Swanson, C. P. Lin, J. S. Schuman, W. G. Stinson, W. Chang, M. R. Hee, T. Flotte, K. Gregory, and C. A. Puliafito, "Optical coherence tomography," Science **254**, 1178–1181 (1991).
13. J. A. Izatt, E. A. Swanson, J. G. Fujimoto, M. R. Hee, and G. M. Owen, "Optical coherence microscopy in scattering media," Opt. Lett. **19**, 590–592 (1994).
14. J. Kalkman, A. V. Bykov, D. J. Faber, and T. G. Van Leeuwen, "Multiple and dependent scattering effects in Doppler optical coherence tomography," Opt. Express **18**, 3883–3892 (2010).
15. R. K. Wang, "Signal degradation by multiple scattering in optical coherence tomography of dense tissue: a Monte Carlo study towards optical clearing of biotissues," Phys. Med. Biol. **47**, 2281–2299 (2002).
16. V. D. Nguyen, D. J. Faber, E. van der Pol, T. G. van Leeuwen, and J. Kalkman, "Dependent and multiple scattering in transmission and backscattering optical coherence tomography," Opt. Express **21**, 29145–29156 (2013).
17. A. K. Trull, J. van der Horst, J. G. Bijster, and J. Kalkman, "Transmission optical coherence tomography based measurement of optical material properties," Opt. Express **23**, 33550–33563 (2015).
18. Y. Wang and R. K. Wang, "High-resolution computed tomography of refractive index distribution by transillumination low-coherence interferometry," Opt. Lett. **35**, 91–93 (2010).
19. M. R. Hee, E. A. Swanson, J. A. Izatt, J. M. Jacobson, and J. G. Fujimoto, "Femtosecond transillumination optical coherence tomography," Opt. Lett. **18**, 950–952 (1993).
20. L. Li and L. V. Wang, "Optical coherence computed tomography," Appl. Phys. Lett. **91**, 141107 (2007).
21. A. M. Zysk, J. J. Reynolds, D. L. Marks, P. S. Carney, and S. A. Boppart, "Projected index computed tomography," Opt. Lett. **28**, 701–703 (2003).
22. A. C. Kak and M. Slaney, *Principles of Computerized Tomographic Imaging* (SIAM, 2001).
23. D. M. de Bruin, R. H. Bremmer, V. M. Kodach, R. de Kinkelder, J. van Marle, T. G. van Leeuwen, and D. J. Faber, "Optical phantoms of varying geometry based on thin building blocks with controlled optical properties," J. Biomed. Opt. **15**, 025001 (2010).
24. J. van der Horst and J. Kalkman, "Image resolution and deconvolution in optical tomography," Opt. Express **24**, 24460–24472 (2016).
25. M. Kempe, A. Genack, W. Rudolph, and P. Dorn, "Ballistic and diffuse light detection in confocal and heterodyne imaging systems," J. Opt. Soc. Am. A **14**, 216–223 (1997).
26. V. M. Kodach, J. Kalkman, D. J. Faber, and T. G. van Leeuwen, "Quantitative comparison of the OCT imaging depth at 1300 nm and 1600 nm," Biomed. Opt. Express **1**, 176–185 (2010).
27. S. L. Jacques, "Optical properties of biological tissues: a review," Phys. Med. Biol. **58**, R37–R61 (2013).
28. A. Badon, A. C. Boccara, G. Lerosey, M. Fink, and A. Aubry, "Multiple scattering limit in optical microscopy," Opt. Express **25**, 28914–28934 (2017).
29. I. M. Vellekoop and A. Mosk, "Focusing coherent light through opaque strongly scattering media," Opt. Lett. **32**, 2309–2311 (2007).
30. A. P. Mosk, A. Lagendijk, G. Lerosey, and M. Fink, "Controlling waves in space and time for imaging and focusing in complex media," Nat. Photonics **6**, 283–292 (2012).
31. P. Lai, L. Wang, J. W. Tay, and L. V. Wang, "Photoacoustically guided wavefront shaping for enhanced optical focusing in scattering media," Nat. Photonics **9**, 126–132 (2015).

32. C. Ma, X. Xu, Y. Liu, and L. V. Wang, "Time-reversed adapted-perturbation (trap) optical focusing onto dynamic objects inside scattering media," Nat. Photonics **8**, 931–936 (2014).
33. S. Kang, S. Jeong, W. Choi, H. Ko, T. D. Yang, J. H. Joo, J.-S. Lee, Y.-S. Lim, Q.-H. Park, and W. Choi, "Imaging deep within a scattering medium using collective accumulation of single-scattered waves," Nat. Photonics **9**, 253–258 (2015).
34. K. H. Zhou, R. Qian, S. Degan, S. Farsiu, and J. A. Izatt, "Optical coherence refraction tomography," Nat. Photonics **13**, 794–802 (2019).
35. B. Grajciar, M. Pircher, A. F. Fercher, and R. A. Leitgeb, "Parallel Fourier domain optical coherence tomography for in vivo measurement of the human eye," Opt. Express **13**, 1131–1137 (2005).
36. A. K. Trull, J. van der Horst, W. J. Palenstijn, L. J. van Vliet, T. van Leeuwen, and J. Kalkman, "Point spread function based image reconstruction in optical projection tomography," Phys. Med. Biol. **62**, 7784 (2017).
37. C. Pardo-Martin, T.-Y. Chang, B. K. Koo, C. L. Gilleland, S. C. Wasserman, and M. F. Yanik, "High-throughput in vivo vertebrate screening," Nat. Methods **7**, 634–636 (2010).
38. Y. Guo, W. J. Veneman, H. P. Spaink, and F. J. Verbeek, "Three-dimensional reconstruction and measurements of zebrafish larvae from high-throughput axial-view in vivo imaging," Biomed. Opt. Express **8**, 2611–2634 (2017).
39. S. L. Logan, C. Dudley, R. P. Baker, M. J. Taormina, E. A. Hay, and R. Parthasarathy, "Automated high-throughput light-sheet fluorescence microscopy of larval zebrafish," PLOS ONE **13**, e0198705 (2018).
40. Y. Guo, R. C. van Wijk, E. H. J. Krekels, H. P. Spaink, P. H. van der Graaf, and F. J. Verbeek, "Multi-modal 3D reconstruction and measurements of zebrafish larvae and its organs using axial-view microscopy," in *IEEE International Conference on Image Processing (ICIP)* (2017), pp. 2194–2198.
41. J. Kalkman, Zenodo repository, 2020, https://www.doi.org/10.5281/zenodo.4138957.